Effects of wind turbine rotor tilt on large-scale wind farms

Journal of Physics: Conference Series **2767** (2024) 092072 doi:10.1088/1742-6596/2767/9/092072

Effects of wind turbine rotor tilt on large-scale wind farms

Jens H. Kasper and Richard J.A.M. Stevens

Physics of Fluids Group, Max Planck Center Twente for Complex Fluid Dynamics, J.M. Burgers Center for Fluid Dynamics and MESA+ Research Institute, University of Twente, 7500 AE Enschede, The Netherlands

E-mail: j.h.kasper@utwente.nl, r.j.a.m.stevens@utwente.nl

Abstract. Recent studies have explored the use of rotor tilt adjustments to reduce wake losses in wind farms. While downward wake deflection in aligned wind farms has shown promise for significant power gains, the impact of wind farm layout on the effectiveness of tilt strategies is not yet fully understood. Additionally, the effect on downstream farms remains unclear. Our large eddy simulations reveal that a rotor tilt of 20 degrees significantly reduces wake losses in aligned wind farms. For wind farms with 8 turbine rows, we observe an overall increase in wind farm productivity of up to 11%. However, tilting the rotors may decrease power production in staggered wind farms, where wake losses are inherently lower due to the increased spacing between turbines. Our findings also suggest that a downstream wind farm might benefit from an upstream farm implementing rotor tilt, although this advantage is primarily observed in the first row of the downstream farm.

1. Introduction

The performance of wind farms is strongly impacted by wake losses. One recently explored method for reducing such losses involves tilting the turbine rotors; see Figure 1(a). Misalignment between the rotor and inflow induces a pair of counter-rotating vortices, which deflect the wake center away from the turbine [1, 2]. The wake deflects downward for a positive tilt angle γ and upward for negative γ [3, 4]. Particularly, the use of positive tilt in aligned turbine configurations has seen significant attention in recent years as it yields considerable power gains in small wind farms [4, 5, 6, 7]. Cossu [5] found that for wind farms with 3 rows in a pressure-driven atmospheric boundary layer (ABL), overall power output may increase by up to 8% by employing a static rotor tilt. A similar study, including Coriolis forces, revealed power gains of up to 15% [6]. Trigaux et al. [7] reported power gains of up to 14.5% for aligned wind farms with 5 rows in a pressure-driven ABL.

However, these studies focus on the particular scenario of perfectly aligned turbine columns. The effectiveness of tilting largely depends on this particular layout, as it deflects wakes away from turbines positioned directly downstream. Annoni et al. [4] demonstrated that adding a small spanwise offset to a downstream turbine can transform a tilt-induced power gain into a significant power loss. In practice, non-aligned wind farm configurations are common, which raises the question of how well tilt strategies perform in wind farms with different turbine layouts.

Another unexplored topic of interest concerns how rotor tilt will affect neighboring wind farms, through the alteration of wind farm-atmosphere interactions. Tilting the turbine rotors alters the vertical structure of the wind farm wake in the ABL, consequently altering

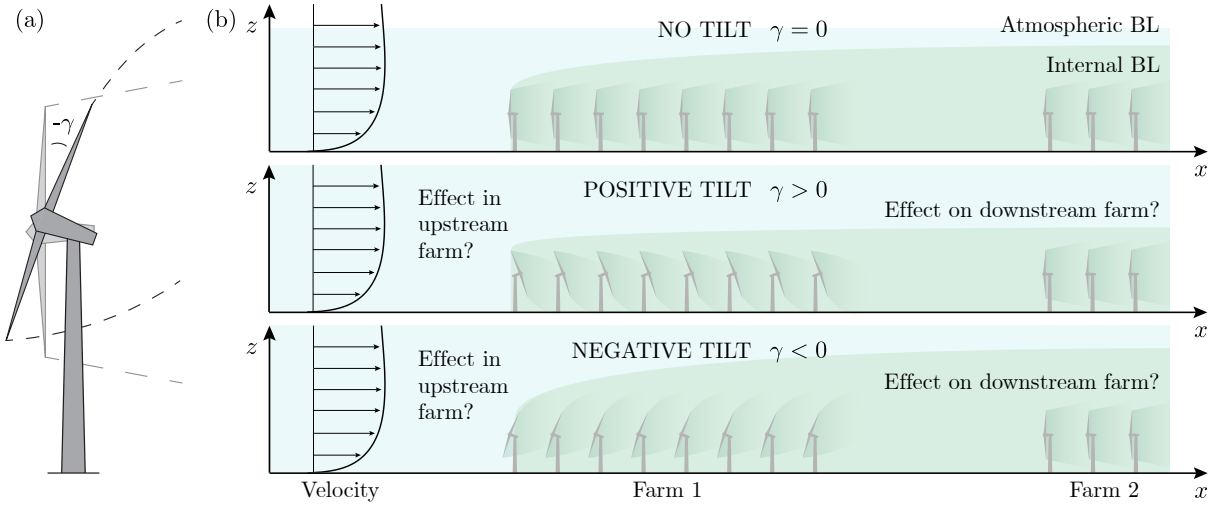

Figure 1. Schematic illustrations outlining the considered research question: how does turbine rotor tilt affect the power production of a large, non-aligned wind farm, as well as that of a neighboring downstream wind farm? (a) Individual turbine at a negative rotor tilt angle γ. (b) Comparison of wind farms with no tilt, positive tilt and negative tilt being employed.

inflow conditions for downstream positioned wind farms. Furthermore, studies have shown the performance of large wind farms depends significantly on the downward turbulent entrainment of momentum from higher up in the atmosphere [8, 9, 10]. It is, therefore, worth exploring whether a wind farm employing a non-zero tilt angle can enhance this entrainment process.

In the present work we use large eddy simulations (LES) to answer the research question: how does turbine rotor tilt impact the performance of a large, non-aligned wind farm, as well as that of a neighboring downstream wind farm? Schematic illustrations outlining the research question are given in Figure 1. It should be noted that tilt could possibly be combined with yaw misalignment (traditional wake steering), to more favourably maneuver the wakes. In this work, we will focus on pure tilt strategies only.

The remainder of this article is structured as follows. In Section 2 we discuss the employed simulation methodology and provide an overview of the considered cases. The characteristics of the undisturbed ABL are addressed in Section 3.1. In Section 3.2 we evaluate the wind farm power production for the different cases, and the flow in and around the wind farms is discussed in Section 3.3. Finally, the article is concluded in Section 4.

2. Methodology

2.1. Governing equations

To study the effect of rotor tilt on wind farms, we perform LES using an in-house code, which is an updated version of the code used by Albertson and Parlange [11]. The code was previously validated and can accurately simulate wind turbine wakes in the ABL [12]. The governing equations considered in our LES, the incompressible equations for mass and momentum conservation, are given by

$$\partial_i \tilde{u}_i = 0, \tag{1}$$

$$\partial_t \tilde{u}_i + \partial_j \left(\tilde{u}_i \tilde{u}_j\right) = -\partial_i \tilde{p}^* - \partial_j \tau_{ij} + \epsilon_{ij3} f_c \left(\tilde{u}_j - U_j\right) + f_i, \tag{2}$$

Here, tildes denote filtered variables, and $i = 1, 2, 3$ correspond to streamwise, spanwise, and vertical directions, respectively. Note that the notations $(x_1, x_2, x_3), (\tilde{u}_1, \tilde{u}_2, \tilde{u}_3)$ and

$(x, y, z), (\tilde{u}, \tilde{v}, \tilde{w})$ are used interchangeably. The resolved velocity field is denoted by $\tilde{u}_i$. The total subgrid-scale (SGS) stress tensor is decomposed as $\tau_{ij}^t = \tau_{ij} + \left(\tau_{kk}^t/3\right)\delta_{ij}$. Here, the deviatoric part is given by $\tau_{ij} = \widetilde{u_i u_j} - \tilde{u}_i\tilde{u}_j$ and is modeled using the anisotropic minimum dissipation model [13, 14]. The trace $\tau_{kk}^t/3$ is absorbed into the modified pressure, defined as $\tilde{p}^* = (\tilde{p} - p_\infty)/\rho_0 + \tau_{kk}^t/3$, with mean pressure p_∞ and hydrostatic density ρ_0. Stresses due to molecular viscosity are neglected. The geostrophic wind velocity is given by $U_i = -\epsilon_{ij3}\partial_j p_\infty/(\rho_0 f_c)$, with alternating unit tensor ϵ_{ij3} and Coriolis frequency f_c. The effects of thermal stratification are not taken into account; the results presented here are obtained for (near)-neutral atmospheric conditions.

We use the actuator disk model (ADM) [15, 16, 17] to model the turbine forces f_i. The ADM has been thoroughly validated, and it enables the simulation of far-wake structures with sufficient accuracy [18, 19]. The total turbine force F_t is given by

$$F_t = \frac{1}{2}\rho C_T U_\infty^2 \frac{\pi}{4} D^2, \tag{3}$$

with air density ρ, thrust coefficient C_T, free stream velocity U_∞ and rotor diameter D. As U_∞ is not well defined for subsequent wind turbine rows, the approximation $C_T U_\infty^2 \approx C_T' U_D^2$ is used in the evaluation of Equation (3). Here, U_D is the disk-averaged resolved velocity, and $C_T' = C_T/(1-a)^2$ is the scaled thrust coefficient, with induction factor a. For details on how U_D is sampled from $\tilde{u}_i$ and how F_t is projected onto the numerical grid as f_i, we refer the reader to Refs. [17, 20, 21, 22].

2.2. Boundary conditions and discretization

We employ periodic boundary conditions in horizontal directions, and at the top of the domain a free-slip boundary condition with zero vertical velocity is applied. The classic logarithmic wind profile [23, 24] is used to enforce a no-slip boundary condition at the bottom of the domain. The corresponding wall stress is modeled as

$$\tau_{i3}^{wall} = -u_*^2 \frac{\tilde{u}_i}{\tilde{u}_r} = -\left[\frac{\tilde{u}_r \kappa}{\ln(z/z_0)}\right]^2 \frac{\tilde{u}_i}{\tilde{u}_r} \tag{4}$$

where u_* is the friction velocity, z_0 is the roughness height, $\kappa = 0.4$ is the von Kármán constant and $\tilde{u}_r = \sqrt{\tilde{u}^2 + \tilde{v}^2}$ is the filtered velocity magnitude at the first grid level [24].

A rectilinear grid is used to discretize the numerical domain. The grid is uniform in streamwise and spanwise directions, comprising $n_x = L_x/\Delta_x$ and $n_y = L_y/\Delta_y$ grid points, respectively. Here L_x and L_y are the domain length and width, and Δ_x and Δ_y are the respective grid resolutions. In vertical direction a uniform grid is used up to a height z_u, with grid spacing Δ_z. Above z_u, the grid is stretched progressively up to the domain height L_z, using a hyperbolic tangent stretching function, to reduce computational overhead.

A second-order central finite difference scheme is used to compute derivatives in the vertical direction, while pseudo-spectral differentiation is used to calculate derivatives in the horizontal directions. We use the 3/2 anti-aliasing method to prevent aliasing errors in the non-linear terms. For the time integration of Equation (2) we use a third-order accurate Adams-Bashforth scheme. A concurrent precursor method [25] is used to prevent any remaining wind farm flow structures at the end of the domain from contaminating the inflow via the periodic boundary conditions. Sampled flow data from a concurrent ABL simulation, without turbines, is used to force the flow in a fringe region in the wind farm domain to the undisturbed state. Due to the Coriolis force, the wind direction changes with height, so streamwise and spanwise fringes are needed.

For the sake of convenience, the use of the tilde, denoting LES filtering, is omitted in the remainder of this work.

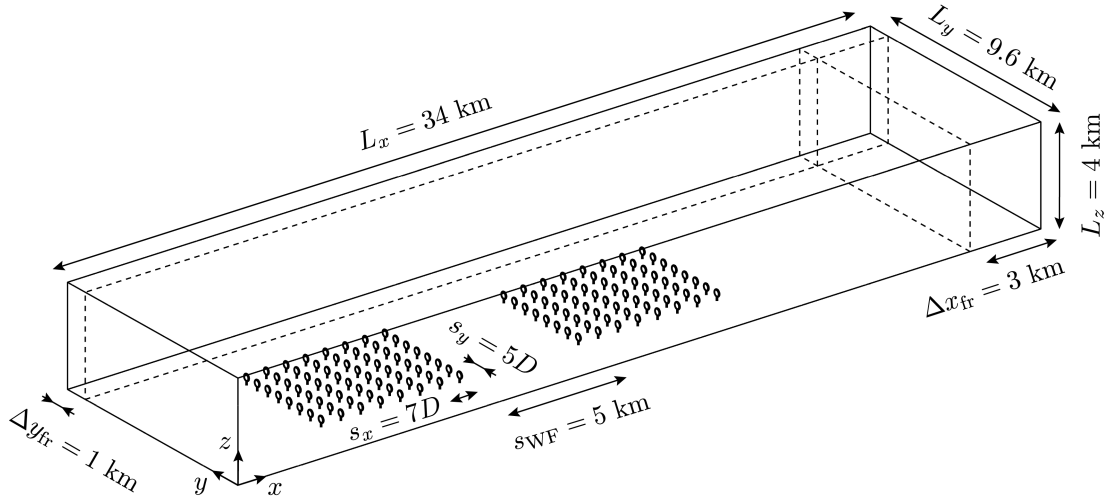

Figure 2. Schematic overview of the computational domain, showing two wind farms with aligned layout.

Table 1. Overview of the considered simulations, documenting wind farm layout and applied rotor tilt γ.

Case	A0	A20	A-20	S0	S20	S-20
Farm 1 layout	aligned	aligned	aligned	staggered	staggered	staggered
Farm 2 layout	aligned	aligned	aligned	staggered	staggered	staggered
Farm 1 tilt γ [°]	0	20	−20	0	20	−20
Farm 2 tilt γ [°]	0	0	0	0	0	0

2.3. Case overview

We evaluate six cases, summarized in Table 1. In each case, two wind farms are considered in the simulation. Both have either an aligned or staggered layout and are a distance $s_{\mathrm{WF}} = 5$ km apart. Both farms consist of 8×8 turbines, each with a rotor diameter of $D = 120$ m and a hub height of $z_h = 100$ m. The turbines all operate at a thrust coefficient of $C_T = 0.75$ and induction factor of $a = 0.25$. The streamwise and spanwise spacing between the turbines is $s_x = 7D$ and $s_y = 5D$, respectively. We vary the rotor tilt angle γ of all turbines in the upstream farm, which is collectively prescribed as either -20, 0, or 20 degrees, where positive γ means downward wake deflection, see Figure 1(a). The turbines in the second farm are always operated at a tilt angle of 0 degrees. Apart from the imposed rotor tilt, the two farms are always identical. This allows direct evaluation of the impact of the tilt strategy on both the upstream and downstream farm.

Figure 2(b) displays a schematic overview of the computational domain. The domain has a size of $L_x \times L_y \times L_z = 34 \times 9.6 \times 4$ km, and is discretized using $n_x \times n_y \times n_z = 1136 \times 640 \times 256$ grid points. The grid resolutions in horizontal directions are $\Delta_x = 30$ m and $\Delta_y = 15$ m. In vertical direction, the grid resolution is $\Delta_z = 10$ m up to $z_u = 1.5$ km, while above z_u the grid is stretched up to a maximum of $\Delta_z = 35$ m. The streamwise and spanwise fringe regions, forcing the precursor flow to the wind farm domain, have a size of $\Delta x_{\mathrm{fr}} = 3$ km and $\Delta y_{\mathrm{fr}} = 1$ km, respectively. We prescribe a geostrophic wind of $|U_i| = 11$ m/s, surface roughness height of $z_0 = 0.002$ m and Coriolis frequency of $f_c = 1.159 \cdot 10^{-4}$ s^{-1}, typical for North Sea conditions. We employ a PID controller that ensures the wind direction at hub height is aligned with the x-axis of the domain [26].

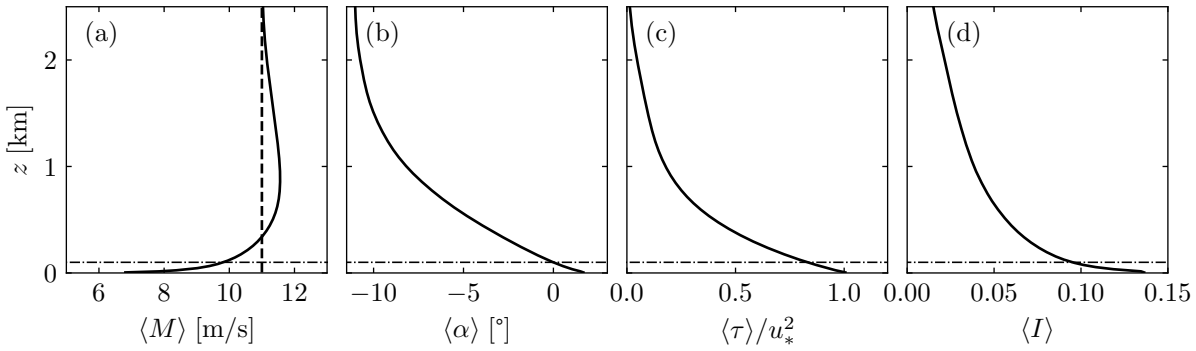

Figure 3. Temporally and horizontally averaged properties of the undisturbed ABL, as a function of height z. (a) Normalized horizontal velocity magnitude $\langle M \rangle$, with the imposed geostrophic wind shown by the dashed line. (b) Wind angle $\langle \alpha \rangle$, (c) shear stress $\langle \tau \rangle$ normalized using friction velocity u_*, and (d) turbulence intensity $\langle I \rangle$. Hub height is indicated by the black dash-dotted line.

The simulations are performed in two stages. First, a spin-up simulation is performed on a coarse domain, discretized by $n_x/2 \times n_y/2 \times n_z$ grid points. Random perturbations are added in the lower portion of the ABL to spin up turbulence. After 7 hours, once the ABL has reached a quasi-steady state, the flow field is interpolated to the full resolution of $n_x \times n_y \times n_z$. Subsequently, the turbines are inserted and the concurrent precursor simulation is run. Statistics are collected after a 1 h adjustment period, from the 8^{th} to the 11^{th} hour.

3. Results

3.1. Boundary layer characteristics

In this section the flow characteristics of the undisturbed ABL are discussed, see Figure 3, to provide context for the atmosphere-wind farm interactions and improve reproducibility of our results. The velocity magnitude $\langle M \rangle = \langle \sqrt{\bar{u}^2 + \bar{v}^2} \rangle$ is presented in Figure 3(a). Here $\langle . \rangle$ denotes a spatial mean, while $\bar{.}$ denotes a temporal average. The imposed geostrophic wind of $|U_i| = 11$ m/s results in a hub height velocity equal to $u_h \approx 9.8$ m/s, and a velocity maximum of 11.6 m/s at $z = 880$ m. Higher up in the atmosphere, the wind velocity approaches the geostrophic wind speed. Figure 3(b) shows the mean wind angle $\langle \alpha \rangle = \langle \tan^{-1}(\bar{v}/\bar{u}) \rangle$ with height. Note that by design $\langle \alpha \rangle = 0°$ at hub height. The wind veer over the rotor disk is roughly 1.3°. The mean turbulent stress $\langle \tau \rangle = \left\langle \sqrt{\left(\overline{u'w'}\right)^2 + \left(\overline{v'w'}\right)^2} \right\rangle$ is depicted in Figure 3(c). It is normalized by the corresponding friction velocity $u_* = 0.35$ m/s. The height of the ABL, based on the mean stress profile (as defined by Kosović and Curry [27]) is $z_{\text{ABL}} \approx 2.1$ km. The mean turbulence intensity $\langle I \rangle = \left\langle \sqrt{\overline{u'^2} + \overline{v'^2}} \right\rangle / \langle M \rangle$ is shown in Figure 3(d). At hub height the turbulence intensity equals $\langle I \rangle = 9.4\%$.

3.2. Power production

The power production $P/P_{1,\gamma=0}$ for all cases is shown in Figure 4. Here, P is the time- and row-averaged power production as a function of turbine row. $P_{1,\gamma=0}$ is the power output of row 1 for the $\gamma = 0$ case. In all aligned cases, depicted in Figure 4(a), the wind farm power curves exhibit similar global trends. The first turbine row has relatively high power production, benefiting from a high-velocity inflow. The second turbine row is waked and consequently experiences considerable wake losses. Further downstream, wake-generated turbulence leads to significant energy entrainment from higher up in the atmosphere, such that the power production slightly

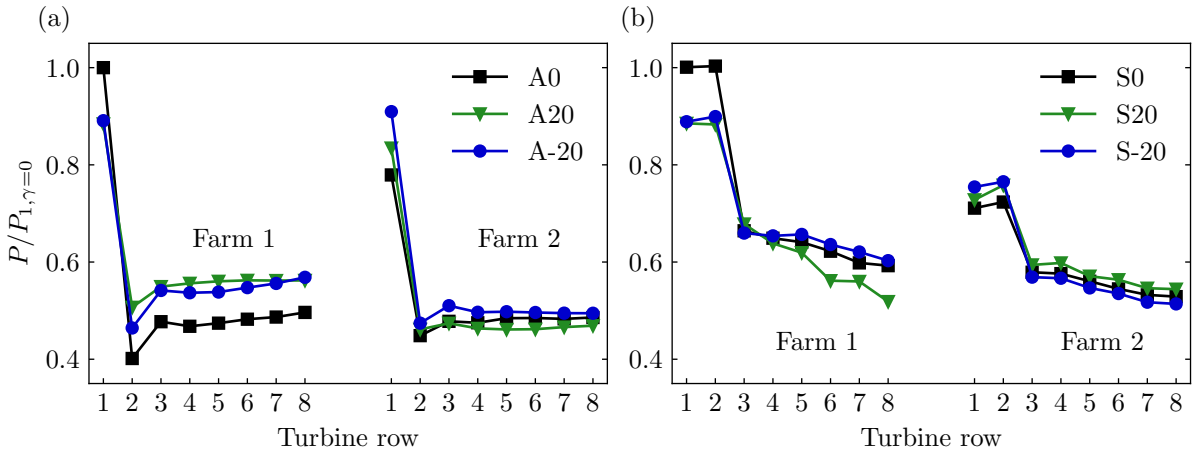

Figure 4. Comparison of the row-averaged turbine power P, normalized by the first-row power $P_{1,\gamma=0}$ of the corresponding no-tilt case, as a function of turbine row. (a) The aligned cases and (b) the staggered cases.

Table 2. Overview of the aerodynamic power generated per farm and in total, for all cases, assuming a power coefficient of $C_P = 0.5$ and air density of $\rho = 1.225$ kg/m^3.

Case	A0	A20	A-20	S0	S20	S-20
Farm 1 power [MW]	110	122	119	148	137	144
Farm 2 power [MW]	106	105	112	122	126	123
Total power [MW]	216	227	232	271	264	267

increases with downstream distance.

An imposed 20-degree tilt induces substantial relative differences in the Farm 1 power production. The first-row power is decreased by roughly 10% in both cases with tilt. This decrease occurs because the turbines encounter the same inflow conditions as in the no-tilt scenario, but are not aligned properly with the inflow. Subsequent turbine rows experience reduced wake losses due to tilt-induced wake deflections. In these rows we observe significant power gains ranging from $0.06P_{1,\gamma=0}$ to $0.11P_{1,\gamma=0}$. In Farm 2, situated 5 km behind Farm 1, the beneficial effects of tilt are still felt in the first turbine row. As the turbines in Farm 2 are not tilted, the benefit diminishes quickly further downstream.

Figure 4(b) displays the power production of turbines in the staggered wind farms. In this layout, turbines in the second row are not affected by the wakes of the first-row turbines. Additionally, the impact of wakes in the third row is lower, due to the larger effective streamwise spacing between turbines. Nonetheless, as wake effects accumulate across the wind farm, power production gradually decreases, eventually reaching levels comparable to those in the aligned case. The figure indicates that tilting turbines offers no benefit in this wind farm layout. The advantages of wake deflection do not compensate for the lost power production due to tilting the wind turbines. This is especially noticeable for the S20 case, where a notable reduction in power is observed in the downstream rows. However, the power production in the first row(s) of Farm 2 still increases, as the wake from Farm 1 is deflected away from hub height.

Table 2 presents an overview of the total aerodynamic power production per wind farm, assuming an aerodynamic power coefficient of $C_P = 0.5$ and air density of $\rho = 1.225$ kg/m^3. In the aligned cases, positive and negative tilt yield a net power gain for Farm 1 of 11% and 8 %, respectively. Here, the power gains for the downstream turbines substantially outweigh the losses

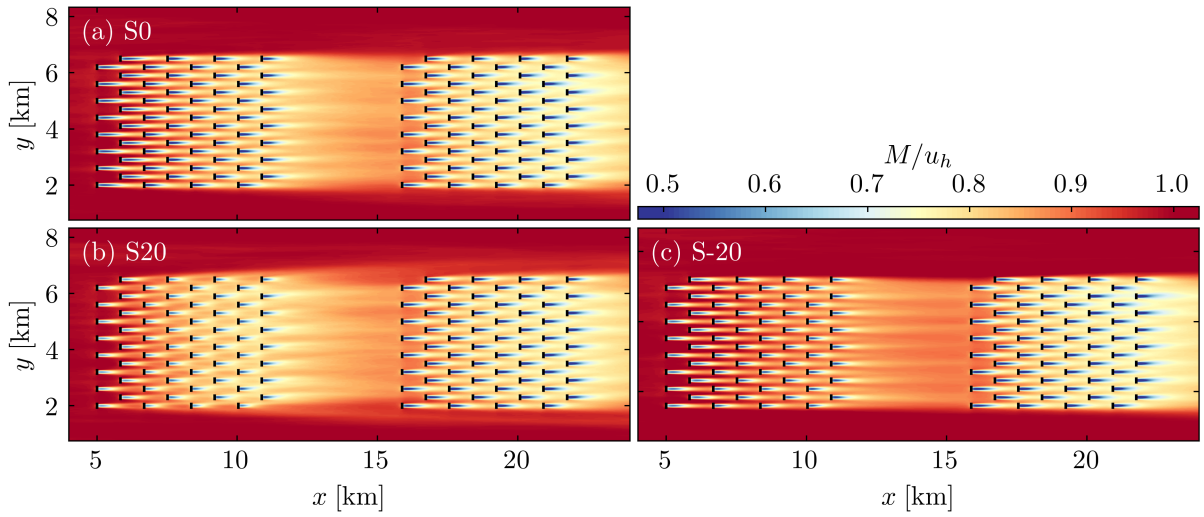

Figure 5. Contour plots of the mean velocity fields M in the x,y-plane at hub height, for the staggered cases. (a) The no-tilt case S0, (b) the positive tilt case S20, and (c) the negative tilt case S-20.

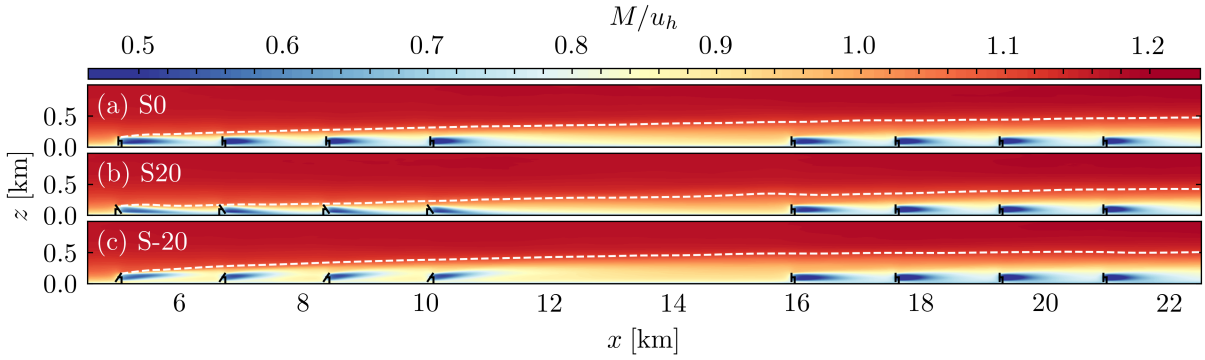

Figure 6. Contour plots of the mean velocity fields M in the x,z-plane at the first turbine column, for the staggered cases. (a) The no-tilt case S0, (b) the positive tilt case S20, and (c) the negative tilt case S-20. The IBL height is depicted by the white dashed line.

experienced by the first row. For the negative tilt case A-20, the effect of tilt on the downstream Farm 2 is beneficial, while for case A20 the tilt is slightly harmful. As a result, negative tilt (i.e. upward wake deflection) is most beneficial for the overall production of Farm 1 and Farm 2, increasing power output by about 7%. For the staggered cases, both positive and negative tilt decrease the net performance of Farm 1. Farm 2 still benefits, as it profits from the deflection of the wake of Farm 1. However, since the corresponding power gain is limited to the first two turbine rows, the performance increase in Farm 2 does not outweigh the losses experienced by Farm 1.

3.3. Flow in and around the wind farms

To better understand the differences in wind farm performance discussed in Section 3.2, we evaluate the flow in and around the wind farms. Figure 5 shows top-view visualizations of the time-averaged flow velocity through the wind farms with staggered layouts. In the positive tilt case S20, we observe enhanced lateral expansion of the wakes, with higher velocity streaks

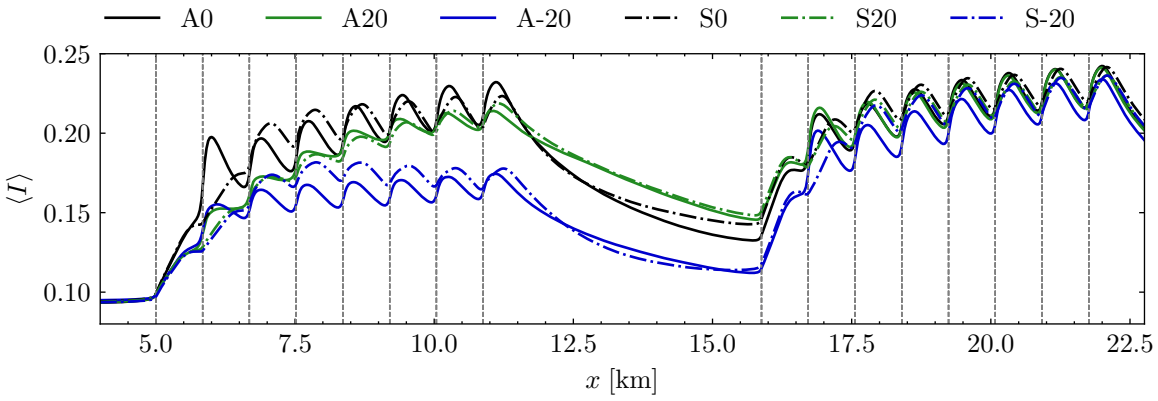

Figure 7. Comparison of the spanwise-averaged turbulence intensity $\langle I \rangle$ at hub height, as a function of distance x, for both the aligned and staggered cases.

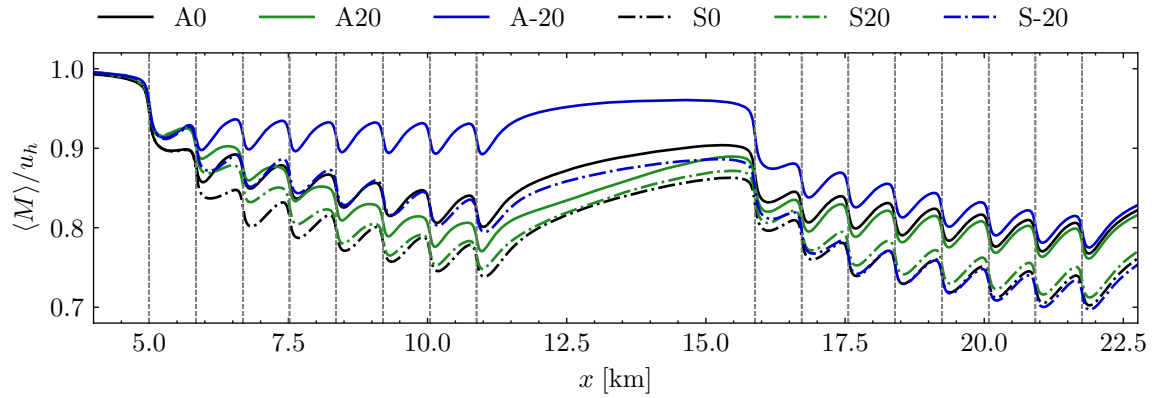

Figure 8. Comparison of the spanwise-averaged flow velocity magnitude $\langle M \rangle$ at hub height, as a function of distance x, for both the aligned and staggered cases.

forming directly behind the turbines, see Figure 5(b). This is a result of the tilt-induced counter-rotating vortex pair present in the wakes [5]. They draw in high velocity air from aloft, and reposition low velocity air laterally, as the ground obstructs downward displacement of air. This makes this tilt strategy highly effective when turbine rows are positioned directly behind preceding rows (aligned layout), but less so when there is an offset (staggered layout), as is reflected in the Farm 1 power production (see Table 2 and Figure 4). In contrast, in the negative tilt case S-20 the vortex pair is reversed, and able to displace low velocity air upward without obstruction. Consequently, the wakes are less pronounced at hub height.

Figure 6 visualizes the flow velocity from a side view taken at the first turbine column. The downward and upward wake deflections due to tilt in Farm 1 are clearly visible. Consequently, compared to case S0, the internal boundary layer (IBL) height is increased in case S-20 and decreased in case S20. Here, we define the IBL height as the height where the ratio of the flow velocity to the inflow velocity at that height reaches 97% [28, 29]. Although a higher IBL height is often associated with increased turbulent transport, case S-20 exhibits no evident enhancement of downward entrainment of energy into the wind farm; Figure 4(b) displays no substantial improvement of the performance of downstream turbines in Farm 1. Figure 7 reveals that deflecting the wake upwards lowers the mean turbulence intensity $\langle I \rangle$ at hub height inside the wind farm, which is an important factor driving energy entrainment [9]. This reduction

in $\langle I \rangle$ at hub height appears to offset the beneficial effect of a higher internal boundary layer on the total downward energy entrainment. In other words, the employed negative tilt induces vertical wake deflection, but does not necessarily promote vertical wake expansion. We observe that differences in turbulence intensity between the tilt and no-tilt cases persist and remain significant far downstream of Farm 1. As the flow enters Farm 2, the additional wake-generated turbulence starts to dominate $\langle I \rangle$. At the end of Farm 2 the turbulence intensity has become nearly equal in all considered cases.

Figure 8 shows the velocity magnitude averaged over the spanwise extent of the wind farm $\langle M \rangle$ at hub height as a function of x. The flow velocity throughout Farm 1 remains significantly higher in the negative tilt cases A-20 and S-20, compared to the corresponding no-tilt and positive tilt cases. In other words, in these cases there remains a significant surplus of kinetic energy available to be extracted at hub height within the wind farm. This indicates that the employed control strategy is likely still far from optimized, although downstream turbine power gains are already obtained in Farm 1 in these cases, as shown in Figure 4. Similar to the turbulence intensity, we find that differences in flow velocity persist behind Farm 1, but as the flow progresses through Farm 2 these differences diminish quickly.

4. Conclusion

We performed LES to evaluate the effects of wind turbine rotor tilt on wind farms with 8×8 turbines. Specifically, we compared the efficacy of positive, negative, and no-tilt strategies in both aligned and staggered wind farms, and evaluated their impact on a downstream wind farm. We found that employing a 20-degree positive or negative rotor tilt is beneficial in aligned wind farm layouts, increasing overall farm performance by 11% and 8%, respectively. However, implementing rotor tilt strategies in staggered wind farms is less beneficial and can even reduce overall wind farm performance. Future work could explore whether using yaw could enhance the effectiveness of tilt strategies. A downstream wind farm may benefit from the turbines in the upstream farm being tilted, although the effect is primarily observed in the first row(s) of the downstream farm.

Our findings demonstrate that applying a uniform static positive or negative rotor tilt to all turbines in a wind farm does not improve large-scale downward energy entrainment. While a negative tilt does raise the height of the internal boundary layer, it simultaneously reduces the turbulence intensity at hub height. The resultant effect produces no additional energy entrainment compared to the no-tilt scenario. However, we observed a significant increase in the mean velocity inside the wind farm when negative tilt is employed. This suggests that optimization of power gains may be possible by employing more sophisticated tilt strategies, which could harness these additional velocity resources. Therefore, we recommend further research in this area. Additionally, we recommend future research on how the efficacy of tilt strategies is affected by atmospheric stratification.

Acknowledgments

This project has received funding from the European Research Council under the European Union's Horizon 2020 research and innovation program (Grant No. 804283). We acknowledge the Dutch national e-infrastructure of SURFsara, a subsidiary of SURF cooperation, the collaborative ICT organisation for Dutch education and research. We also acknowledge EuroHPC JU for awarding this project access to Discoverer, hosted by Sofia Tech Park.

References

[1] Bastankhah M and Porté-Agel F 2016 Experimental and theoretical study of wind turbine wakes in yawed conditions *J. Fluid Mech.* **806** 506–541

[2] Howland M F, Bossuyt J, Martínez-Tossas L A, Meyers J and Meneveau C 2016 Wake structure in actuator disk models of wind turbines in yaw under uniform inflow conditions *J. Renew. Sustain. Energy* **8** 043301
[3] Fleming P A, Gebraad P, Lee S, van Wingerden J W, Johnson K, Churchfield M J, Michalakes J, Spalart P and Moriarty P 2014 Evaluating techniques for redirecting turbine wakes using SOWFA *Renew. Energy* **70** 211–218
[4] Annoni J, Scholbrock A, Churchfield M and Fleming P 2017 Evaluating tilt for wind farms *Proc. of the American Control Conf. (Seattle)* 717–722
[5] Cossu C 2021 Replacing wakes with streaks in wind turbine arrays *Wind Energy* **24** 345–356
[6] Cossu C 2021 Evaluation of tilt control for wind-turbine arrays in the atmospheric boundary layer *Wind Energy Sci.* **6** 663–675
[7] Trigaux F, Moens M, Chatelain P and Winckelmans G 2020 Tilted wind turbines in farm configuration for improved global efficiency *J. Phys.: Conf. Ser.* **1618** 062035
[8] Stieren A, Kasper J H, Gadde S N and Stevens R J A M 2022 Impact of negative geostrophic wind shear on wind farm performance *PRX Energy* **1** 023007
[9] Stevens R J A M and Meneveau C 2017 Flow structure and turbulence in wind farms *Annu. Rev. Fluid Mech.* **49** 311–339
[10] Porté-Agel F, Bastankhah M and Shamsoddin S 2020 Wind-turbine and wind-farm flows: A review *Boundary-Layer Meteorol.* **74**(1) 1–59
[11] Albertson J D and Parlange M B 1999 Surface length-scales and shear stress: implications for land-atmosphere interaction over complex terrain *Water Resour. Res.* **35** 2121–2132
[12] Gadde S N, Stieren A and Stevens R J A M 2021 Large-eddy simulations of stratified atmospheric boundary layers: Comparison of different subgrid models *Boundary-Layer Meteorol.* **178** 363–382
[13] Rozema W, Bae H J, Moin P and Verstappen R 2015 Minimum-dissipation models for large-eddy simulation *Phys. Fluids* **27** 085107
[14] Abkar M, Bae H and Moin P 2016 Minimum-dissipation scalar transport model for large-eddy simulation of turbulent flows *Phys. Rev. Fluids* **1** 041701
[15] Jimenez A, Crespo A, Migoya E and Garcia J 2007 Advances in large-eddy simulation of a wind turbine wake *J. Phys.: Conf. Ser.* **75** 012041
[16] Jimenez A, Crespo A, Migoya E and Garcia J 2008 Large-eddy simulation of spectral coherence in a wind turbine wake *Environ. Res. Lett.* **3** 015004
[17] Calaf M, Meneveau C and Meyers J 2010 Large eddy simulations of fully developed wind-turbine array boundary layers *Phys. Fluids* **22** 015110
[18] Stevens R J A M, Gayme D F and Meneveau C 2016 Generalized coupled wake boundary layer model: applications and comparisons with field and LES data for two real wind farms *Wind Energy* **19** 2023–2040
[19] Wu Y T and Porté-Agel F 2011 Large-eddy simulation of wind-turbine wakes: Evaluation of turbine parametrisations *Boundary-Layer Meteorol.* **138** 345–366
[20] Calaf M, Parlange M B and Meneveau C 2011 Large eddy simulation study of scalar transport in fully developed wind-turbine array boundary layers *Phys. Fluids* **23** 126603
[21] Stevens R J A M, Martínez-Tossas L A and Meneveau C 2018 Comparison of wind farm large eddy simulations using actuator disk and actuator line models with wind tunnel experiments *Renew. Energy* **116**(A) 470–478
[22] Shapiro C R, Gayme D F and Meneveau C 2019 Filtered actuator disks: Theory and application to wind turbine models in large eddy simulation *Wind Energy* **22**(10) 1414–1420
[23] Monin A S and Obukhov A M 1954 Basic laws of turbulent mixing in the surface layer of the atmosphere *Tr. Akad. Nauk SSSR Geophiz. Inst.* **24** 163–187
[24] Bou-Zeid E, Meneveau C and Parlange M B 2005 A scale-dependent Lagrangian dynamic model for large eddy simulation of complex turbulent flows *Phys. Fluids* **17** 025105
[25] Stevens R J A M, Graham J and Meneveau C 2014 A concurrent precursor inflow method for large eddy simulations and applications to finite length wind farms *Renew. Energy* **68** 46–50
[26] Stieren A, Gadde S N and Stevens R J A M 2021 Modeling dynamic wind direction changes in large eddy simulations of wind farms *Renew. Energy* **170** 1342–1352
[27] Kosović B and Curry J A 2000 A large eddy simulation study of a quasi-steady stably stratified atmospheric boundary layer *J. Atmos. Sci.* **57** 1052–1068
[28] Gadde S N and Stevens R J A M 2021 Interaction between low-level jets and wind farms in a stable atmospheric boundary layer *Phys. Rev. Fluids* **6**(1) 014603
[29] Allaerts D and Meyers J 2017 Boundary-layer development and gravity waves in conventionally neutral wind farms *J. Fluid Mech.* **814** 95–130